REPORT DOCUMENTATION PAGE

Form Approved OMB No. 0704-0188

Public reporting burden for this collection of information is estimated to average 1 hour per response, including the time for reviewing instructions, searching existing data sources, gathering and maintaining the data needed, and completing and reviewing this collection of information. Send comments regarding this burden estimate or any other aspect of this collection of information, including suggestions for reducing this burden to Department of Defenses, Washington Headquarters Services, Directorate for Information Operations and Reports (0704-0188), 1215 Jefferson Davis Highway, Suite 1204, Arlington, VA 22202-4302. Respondents should be aware that notwithstanding any other provision of law, no person shall be subject to any penalty for failing to comply with a collection of information if it does not display a currently valid OMB control number. PLEASE DO NOT RETURN YOUR FORM TO THE ABOVE ADDRESS.

1. REPORT DATE (DD-MM-YYYY)	2. REPORT TYPE	3. DATES COVERED (From - To)		
May 2014	Technical Paper	May 2014- June 2014		
4. TITLE AND SUBTITLE		5a. CONTRACT NUMBER		
		In house		
Stability analysis of high-speed boundary	5b. GRANT NUMBER			
		5c. PROGRAM ELEMENT NUMBER		
6. AUTHOR(S)	5d. PROJECT NUMBER			
Alexander V. Fedorov, Vitaly G. Sou	ndakov; Ivett A Leyva	5e. TASK NUMBER		
		5f. WORK UNIT NUMBER		
		Q0AF		
7. PERFORMING ORGANIZATION NAM	E(S) AND ADDRESS(ES)	8. PERFORMING ORGANIZATION REPORT NO.		
Air Force Research Laboratory (AFM	MC)			
AFRL/RQRE				
4 Draco Drive.				
Edwards AFB CA 93524-7160				
9. SPONSORING / MONITORING AGEN		10. SPONSOR/MONITOR'S ACRONYM(S)		
Air Force Research Laboratory (AFN	IC)			
AFRL/RQR				
5 Pollux Drive	11. SPONSOR/MONITOR'S REPORT			
Edwards AFB CA 93524-7048		NUMBER(S)		
		AFRL-RQ-ED-TP-2014-129		

12. DISTRIBUTION / AVAILABILITY STATEMENT

Distribution A: Approved for Public Release; Distribution Unlimited

13. SUPPLEMENTARY NOTES

Technical paper presented at 44th AIAA Fluid Dynamics Conference, Atlanta, GA, 16-20 June 2014. PA#14249

14. ABSTRACT

Stability analyses of high-speed boundary-layer flow past a 5 half angle sharp cone with the wall-normal injection of air through a porous strip are performed using Navier-Stokes solutions for the mean flow and linear stability theory. The configuration and free-stream parameters are chosen to be similar to the experiments, which were carried out at Caltech's T5 shock tunnel to investigate the effect of CO2 injection on laminar-turbulent transition. The analysis is focused on pure aerodynamic effects in the framework of perfect gas model. It is shown that the injection leads to destabilization of the Mack second mode in the nearfield relaxation region and its stabilization in the far-field relaxation region. To reduce the destabilization effect it was suggested to decrease the injector surface slope or use suction blowing of zero net injection. However, the en computations showed that these modifications did not improve the injector performance in the near-filed region in general. For special cases of low injection rates in which the N-factors in the near field region are below the critical level, shaping can produce a significant stabilization in the mid- and far-field regions.

15. SUBJECT TERMS

16. SECURITY CLASSIFICATION OF:		17. LIMITATION OF ABSTRACT	18. NUMBER OF PAGES	19a. NAME OF RESPONSIBLE PERSON Ivett Leyva	
a. REPORT	b. ABSTRACT	c. THIS PAGE	SAR	19	19b. TELEPHONE NO (include area code)
Unclassified	Unclassified	Unclassified			5-5817

Stability analysis of high-speed boundary-layer flow with gas injection

Alexander V. Fedorov* and Vitaly G. Soudakov†

Moscow Institute of Physics and Technology, Zhukovsky, 140180, Russia

Ivett A. Leyva[‡]
Air Force Research Laboratory, Edwards AFB, California, 93536

Stability analyses of high-speed boundary-layer flow past a 5° half angle sharp cone with the wall-normal injection of air through a porous strip are performed using Navier-Stokes solutions for the mean flow and linear stability theory. The configuration and free-stream parameters are chosen to be similar to the experiments, which were carried out at Caltech's T5 shock tunnel to investigate the effect of CO₂ injection on laminar-turbulent transition. The analysis is focused on pure aerodynamic effects in the framework of perfect gas model. It is shown that the injection leads to destabilization of the Mack second mode in the near-field relaxation region and its stabilization in the far-field relaxation region. To reduce the destabilization effect it was suggested to decrease the injector surface slope or use suction-blowing of zero net injection. However, the e^N computations showed that these modifications did not improve the injector performance in the near-filed region in general. For special cases of low injection rates in which the N-factors in the near field region are below the critical level, shaping can produce a significant stabilization in the mid- and far-field regions.

Nomenclature

= phase speed cMMach number minjection total mass rate Reynolds number Re pressure pTtemperature axial and radial velocity components 11. 11 Namplification factor streamwise wave number α β azimuthal wave number boundary layer thickness boundary layer displacement thickness δ^* kinematic viscosity σ spatial growth rate angular frequency **Superscripts** dimensional **Subscripts** = free stream

^{*} Associate Professor, Dept. of Aeromechanics and Flight Engineering, e-mail: afedorov55@gmail.com, Associate Fellow AIAA

[†] Associate Professor, Department of Aeromechanics and Flight Engineering, e-mail: vit_soudakov@mail.ru, Member AIAA

[‡]Technical Advisor, AFRL/RQRE, Edwards AFB, California, Associate Fellow AIAA

I. Introduction

It is well known that laminar-turbulent transition on slender bodies in a hypersonic flow at small angles of attack is caused by amplification of acoustic waves trapped in the boundary layer [1,2]. Non-equilibrium effects such as molecular vibration and dissociation can damp acoustic disturbances [3,4]. Carbon dioxide has been found to be well suited to absorb acoustic energy in an enthalpy range relevant to realistic applications [5]. These findings point to the potential beneficial application of adding carbon dioxide into boundary-layer flows in order to delay transition onset. Experimentally, this is attempted by injecting CO_2 into the boundary layer through the wall.

In Ref. [6], three injection schemes were studied both as passive trips with no injection and as active trips with CO₂ injection. The first injector had four rows of 36 orifices. The second injector was derived from the former one by only keeping the fourth or most downstream row of orifices. The third injector consisted of a micro-porous section. It was found that the four-row injector tripped the boundary layer to fully turbulent values near the last row of orifices. The transition Reynolds number with the one-row injector was decreased by more than 50% as compared to the smooth cone. Therefore, while not as efficient as the four-row injector, one row of holes still caused early transition. A porous injector was also tested and did not result in early transition when tested without injection.

Due to the tendency of the discrete jets to cause transition, further studies were focused on the porous injector. The numerical simulations [7] predicted that transition will occur immediately following the injection of cold carbon dioxide. The test cases with air and nitrogen as the test gas suggested the momentum of the injection plays a dominant role in the amount of amplification seen immediately downstream due to the inefficient heating of the injected CO₂. To remedy this, the injected carbon dioxide was pre-heated, resulting in a reduction of amplification in the post-injection region. Despite this reduction, the stability analyses still predicted transition to occur earlier on the cone as compared to the case without injection. To isolate the effects of non-equilibrium processes on the disturbances, a second case involving a similar cone with a longer transpiration interval was tested. For this case, the stability analyses predicted a window of carbon dioxide injection resulting in a reduction of amplification and thus a delay in transition. In Ref. [8], transition delays were documented in shots with CO₂ injection. The data showed a general trend of increasing delay with injection rate, before a sharp drop-off at the highest injection rate. However, the transition delay was smaller than that observed in the free-stream with CO₂.

The foregoing studies indicate that the injector performance essentially depends on the balance between the stabilizing effect of carbon dioxide and the destabilizing effect of blowing. The emphasis of this paper is to study the destabilizing effects of the injection process and try to minimize them by seeking optimal distributions of the blow rate and/or shaping of the injection region. The feasibility studies of different blowing configurations use the perfect gas model as a first step. Therefore, the area of most applicability from these studies is near the injection point where aerodynamic effects are most important and the perfect-gas model is suitable since the injected gas is relatively cold and not in vibrational or chemical non-equilibrium. Further downstream, where the injected flow is heated and it can effectively damp acoustic instabilities, the perfect gas model overestimates the disturbance growth rates and, thereby, under-predicts the injector performance. Once the most promising injector configurations are selected from this study, further computations need to be made of the stabilizing effects of CO₂ downstream of the injection region and experiments need to be performed in a high-enthalpy shock tunnel to confirm those predictions.

The following cases are considered: A) Baseline configuration – a 5° half-angle sharp cone at zero angle of attack with normal-wall blowing through a porous wall strip. This configuration is similar to that tested at Caltech's T5 shock tunnel [6,8]. B) Configuration with shaping of the injection region; C) Configuration with the normal-wall suction and blowing with zero net injection. For each case the laminar basic flow is computed using the in-house Navier-Stokes code HSFlow, and stability analyses are performed in the framework of linear stability theory (LST) using the in-house LST code. These tools were successfully exploited for stability and receptivity studies of high-speed boundary-layer flows [9-12].

II. Baseline configuration and numerical approach

As a first step, we consider the baseline configuration shown in Figure 1. A 5° half-angle sharp cone has the region $128~\mathrm{mm} < x^* < 169~\mathrm{mm}$, where air at the wall temperature is uniformly injected in the normal wall direction. In our computations, the injection total mass rate ranged from 0 g/s to 13.5 g/s, where the upper limit approximately equals the double mass rate of the incoming boundary-layer flow.

The free-stream parameters correspond to the free-stream conditions of Run 2540 in the GALCIT T5 shock tunnel [7]: test gas is air, Mach number $M_{\infty}=5.3$, static temperature $T_{\infty}^*=1323.77$ K, static pressure $p_{\infty}^*=21993$ Pa, density $\rho_{\infty}^*=0.05788$ kg/m³, and wall temperature $T_{w}^*=293$ K. The cone length measured along the cone axis is $L^*=1$ m. Hereafter asterisks denote dimensional quantities. The Reynolds number based on cone length is $\mathrm{Re}_{\infty L}=4.57\cdot 10^6$.

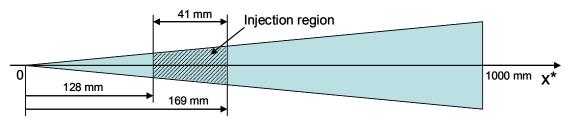


Figure 1. A 5° half-angle sharp cone with the injector – baseline configuration.

Calculations of the basic flow were performed using the in-house Navier-Stokes code HSFlow for perfect gas of Prandtl number $\Pr=0.72$, specific heat ratio $\gamma=1.4$ and Sutherland viscosity-temperature dependence with the Sutherland constant being 110.4 K. The flow variables are made nondimensional using the free-stream parameters and the cone length L^* . Pressure is scaled using the doubled free-stream dynamic pressure $\rho_\infty^* U_\infty^{*2}$, where U_∞^* is free-stream velocity. The computational domain is a rectangle. Its bottom boundary lies on the cone surface, and the upper boundary lies in the free stream above the cone-induced shock. The boundary conditions on the cone surface are the no-slip condition and the isothermal condition $T=T_w$. On the inflow and upper boundaries, the conditions correspond to the undisturbed free stream. On the outflow boundary, the unknown dependent variables are extrapolated using the linear approximation.

The problem is solved numerically using the implicit second-order finite-volume method described in [9]. The two-dimensional (axisymmetric) Navier-Stokes equations are approximated by a shock-capturing scheme that allows for modeling of flow non-uniformities induced by the injector. The advection terms are approximated by the third-order WENO scheme [13] to decrease the numerical dissipation. The code algorithm as well as its implementations and validations are discussed in [9]. The grid convergence study showed that the basic laminar flow can be computed with sufficiently high accuracy using 597×649 grid. This grid is clustered in the direction normal to the cone surface so that the boundary-layer region contains approximately 50% of nodes. To resolve flow non-uniformities in the vicinity of injector, the grid is also clustered in the streamwise direction near the injection boundaries.

The mean flow profiles were used for the local-parallel stability analysis. The boundary-layer disturbance is considered in the wave form $\mathbf{q}(y)\exp(i\alpha x+i\beta z-i\omega t)$, where ω is angular frequency and α,β are streamwise and azimuthal components of the wavenumber vector, t is time. The vector \mathbf{q} consists of the eigenfunctions of velocity components u,v,w, pressure p and temperature T'. For each x-station the linear stability equations are solved using a 4th-order Runge-Kutta scheme and a Gram-Schmidt orthonormalization procedure. For the temporal stability problem, $\omega(\alpha,\beta,x)$ is a complex eigenvalue while α,β are real parameters. For the spatial stability problem, $\alpha(\omega,\beta,x)$ is a complex eigenvalue while β,ω are real parameters. The eigenvalues of discrete spectrum are calculated with the help of a shooting/Newton-Raphson procedure. The downstream amplification factors $N(x,\omega,\beta)$ are computed using solutions of the spatial stability problem

$$N(x,\omega,\beta) = \int_{x_0(\omega,\beta)}^x \sigma(\omega,\beta,x)dx,$$
 (1)

where $\sigma = -\alpha_i$ is the spatial growth rate, and x_0 is the neutral point on the lower neutral branch. Hereafter the subscript 'i' denotes the imaginary part of a complex quantity and 'r' denotes the real part. Stability computations are performed with the assumption that the second (bulk) viscosity is zero.

III. Results for the baseline configuration

The mean flow fields of static pressure and radial velocity are shown in Figure 2a,b for the case of injection with the total mass rate $m=13.5\,$ g/s (the nondimensional mass flow rate is $\rho_w v_w = (\rho_w^* v_w^*)/(\rho_\infty^* v_\infty^*) = 0.0181$). The close up views of axial velocity, static pressure and temperature fields in the injector vicinity are shown in Figure 3, where the dashed lines indicate the injection boundaries. It is seen that the normal-wall blowing displaces the boundary layer and induces compression waves emanating from the upstream boundary of the injector (red color in Figure 3b). A cold dead-flow layer is formed near the wall. Its thickness is of the order of the shear-layer thickness. Owing to the mixing process this layer gets thinner and it is ultimately swallowed by the shear layer in the mid stations $x \approx 0.6$. This trend is clearly seen in Figure 4 where profiles of the streamwise velocity and temperature are shown in various x-stations. Figure 5 shows the near-wall layer thickness $\delta(x)$ determined by the condition $U(\delta) = 0.99U_e$. After a sharp peak in the injection region, $\delta(x)$ decreases and slowly approaches the no-blow distribution. These CFD data demonstrate that the injection strongly affects the near-wall flow not only near the injector but also in a long post-injection region which is called hereafter as a relaxation region.

To get insight into stability of the near-wall layer with injection, we start with the temporal stability analysis for the mean flow profiles in the station x=0.298 which lies in the middle of the relaxation region. The flow parameters are non-dimensionlized using their values at the upper edge of near-wall layer, the length scale is the displacement thickness δ^* and the time scale is δ^* / U_e^* . In the considered herein x-station, the local Mach number is $M_e \approx 5$ and the Reynolds number $\mathrm{Re}_{s^*} = \delta^* U_e^* / \nu_e^* \approx 8074$.

Using a global search for eigenvalues we found seven unstable modes whose increments $\omega_i(\alpha)$ and phase speeds $c_r(\alpha) = \omega_r(\alpha) / \alpha$ are plotted in Figure 6. The computations were performed for plane waves of $\beta = 0$. Figure 7 shows the pressure eigenfunctions p(y) for modes 0, 1, 2 and 3 with the wavenumber α corresponding to maximal increments ω_i for each mode. These eigenfunctions indicate that we are dealing with trapped acoustic waves propagating in a waveguide formed between the wall and the relative sonic line $y = y_a : U(y_a) = c_r - a(y_a)$, where a is local speed of sound [2]. In the waveguide region, $0 < y < y_a$, where the mean flow is supersonic relative to the disturbance phase velocity, the eigenfunction $p_n(y)$ of mode n oscillates versus y so that the oscillation phase is approximately $\pi / 4 + n\pi$, $n = 0,1,\ldots$. Outside the waveguide ($y > y_a$) the eigenfunction decays exponentially. In the Mack terminology, mode 0 corresponds to the second mode, mode 1 – to the third mode etc. Because of relatively thick dead-flow layer the wave guide is essentially thicker and the number of unstable acoustic modes is larger than in the no-blow case.

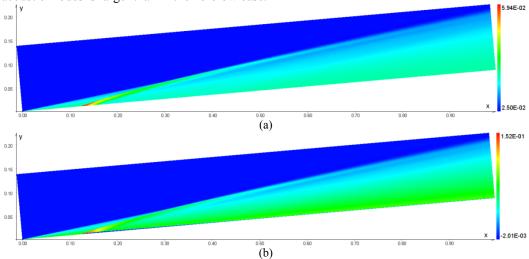


Figure 2. Basic flow fields for the nondimensional static pressure (a), and radial velocity (b), the injection total mass rate $m=13.5\,$ g/s.

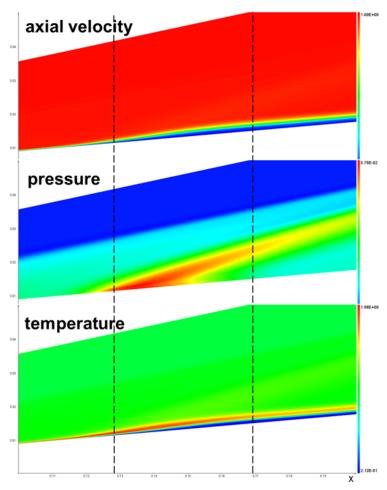


Figure 3. Basic flow fields for the axial velocity, pressure and temperature in the vicinity of injector, the injection total mass flow rate $m=13.5\,$ g/s. The dashed lines show the injection boundaries.

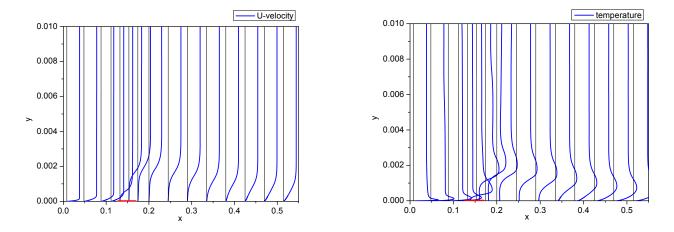


Figure 4. Profiles of the streamwise velocity U(y) and temperature T(y) at various x-stations, the injection total mass rate $m=13.5\,$ g/s, the injection region is shown by the red line.

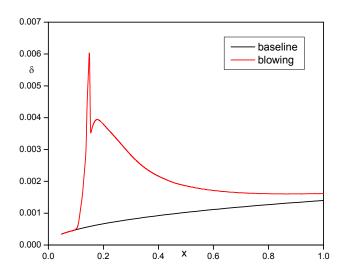


Figure 5. The near-wall layer nondimensional thickness in the no-blow case (black line) and in the case of injection with $m=13.5\,$ g/s (red line).

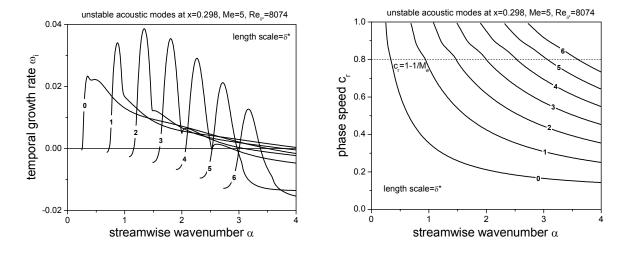
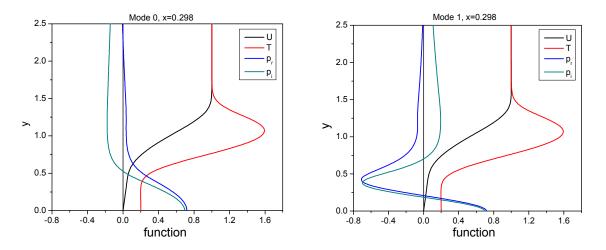


Figure 6. Increments $\omega_i(\alpha)$ and phase speeds $c_r(\alpha)$ of seven unstable modes at x=0.298, $\beta=0$.



Distribution A: Approved for public Release; distribution unlimited

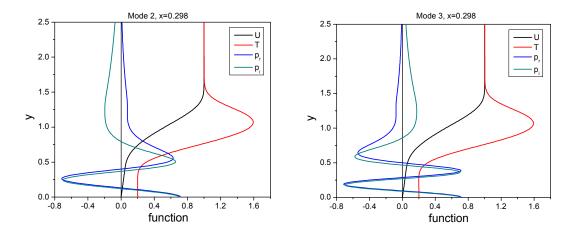


Figure 7. The pressure eigenfunctions $p_r(y)$ and $p_i(y)$ for modes 0, 1, 2 and 3 at (ω,α) corresponding maximal ω_i . The red and black lines show the mean-flow profiles of streamwise velocity U(y) and temperature T(y), respectively.

It turned out that the phase speeds of acoustic instabilities are quite small compared with the no-blow case. As shown in Figure 8, the instabilities are observed in a wide range of c_r and their eigenvalues are close to the branches of slow acoustic waves of the continuous spectrum. The eigenfunctions of such slow modes oscillate outside the boundary layer with very weak damping (Figure 9). This unusual behavior may lead to significant increase of receptivity to free-stream acoustic disturbances.

Note that maximal temporal instability corresponds to mode 2 which is the Mack fourth mode (Figure 6). However the spatial stability analysis leads to the different conclusion. Figure 10 shows that the spatial growth rates $\sigma(\omega)$ are maximal for mode 0 corresponding to the Mack second mode – typical for hypersonic boundary-layer flows. This switch over is associated with abnormal behavior of the group velocities of the considered unstable modes.

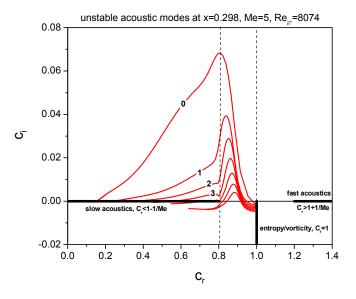


Figure 8. The phase speed trajectories (red lines) of unstable modes in the complex $\,c\,$ plane, the branches of continuous spectrum are shown by the black lines.

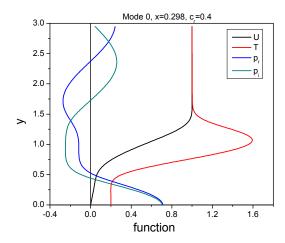


Figure 9. Eigenfunctions $p_r(y)$ and $p_i(y)$ of mode 0 (Mack second mode) at the phase speed $c_r=0.4$. The red and black lines show the mean flow profiles of streamwise velocity U(y) and temperature T(y), respectively.

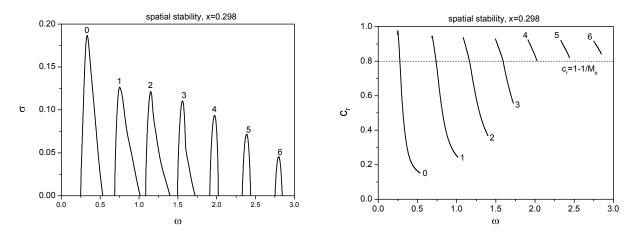


Figure 10. The growth rates $\sigma(\omega)$ and phase speeds $c_r(\omega)$ of seven unstable modes at x=0.298, $\beta=0$.

Figure 11 shows distributions of maximal growth rates $\sigma_{\max}(x) = \max_{\omega} \sigma(\omega, x)$ for the five unstable modes in the relaxation region. In the all x-stations considered, the most unstable is mode 0. Computations for oblique waves, $\beta \neq 0$, showed that their growth rates are smaller than in the case of $\beta = 0$. These findings allow us to restrict further parametric studies to the Mack second mode of $\beta = 0$, which is called hereafter as Mack mode. Note that the injection leads to significant destabilization of the Mack mode in a relatively long region (compare the black and orange lines in Figure 11).

Distributions of the Mack mode growth rates (left plot) at various frequencies (right plot) are shown in Figure 12 for the no-blow case (blue lines) and for the case with injection of $m=13.5\,$ g/s (black lines). The corresponding distributions of N-factors are shown in Figure 13. As expected, the injection destabilizes the Mack mode in the relaxation region that gives a local maximum of the N-factor envelope at $x\approx0.3\,$. Further downstream the maximal growth rates remain higher than in the no-blow case. However the width Δx of unstable regions is narrowed down which leads to decreasing of the integral amplification. As a result the N-factor envelope is lower than that of the no-blow case in the range $0.35 < x < 0.75\,$. In the far-field region $x>0.6\,$ the mean flow is almost parallel and the growth rates weakly depend on x. This causes a steep rise of the N-factor envelope. Eventually this envelope crosses that of no-blow case at $x\approx0.75\,$.

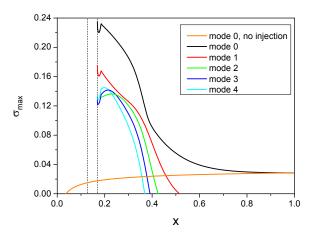


Figure 11. Distributions of maximal growth rates along the relaxation region in the case of injection with m=13.5 g/s; dashed lines show the injector boundaries; the orange line shows the baseline case without injection; $\beta=0$.

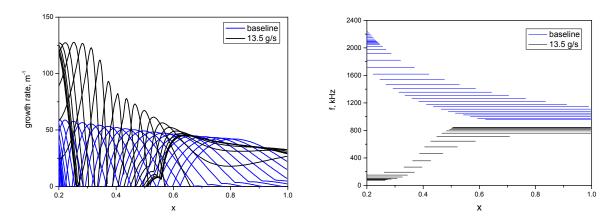


Figure 12. Growth rates and frequencies of the Mack mode for the no-blow (baseline) case (blue lines) and the case with injection of $m=13.5\,$ g/s (black lines).

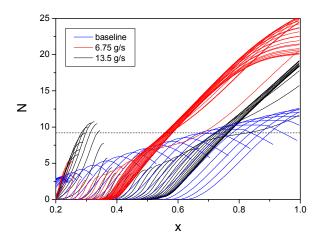


Figure 13. N-factors of the Mack mode for the no-blow (baseline) case (blue lines), the case of $m=13.5\,$ g/s (black lines) and the case of $m=6.75\,$ g/s (red lines); dashed line – $N_{tr}=9.2\,$.

The N factors for the case of $m=6.75\,$ g/s are shown by the red lines in Figure 13. As expected, the near-field maximum of their envelope is significantly smaller than in the case of $m=13.5\,$ g/s. However, the relaxation region becomes shorter and the almost parallel mean flow sets in earlier. The envelope of steep slope is shifted upstream and the N-factors become larger than in the no-blow and $m=13.5\,$ g/s cases for $x>0.5\,$.

Thus, the considered injection leads to destabilization of the near-field relaxation region, stabilization of the midfield relaxation region, and destabilization of the far-field relaxation region where the basic flow is almost parallel. The width and location of these regions as well as the level of stabilization/destabilization effect depend on the injected mass rate. To estimate the transition onset we use hereafter the critical N-factor $N_{tr}=9.2$, which has been derived in Ref. [7] from comparison of the ${\rm e^N}$ computations with the transition measurements on a 5 half-angle sharp cone tested in the GALCIT T5 shock tunnel without injection. For sufficiently large m, at which the maximum of N-factor envelope $N_{\rm max}$ in the near-field relaxation region is higher than the critical $N=N_{tr}$, the transition onset point x_{tr} is predicted to be close to the injector. Decreasing of m weakly affects x_{tr} until $N_{\rm max}$ becomes lower than N_{tr} . At this moment the transition point jumps to the x-station, which may be even downstream from the transition point in the no-blow case; i.e., the premature tripping may be replaced by delay in transition. Further decreasing of m to a certain level can move the transition point upstream. Note that the data in Figure 13 (the first and the second regions of N-factor growth) are consistent with those of Ref. [7] where stability computations were performed for ${\rm CO}_2$ injection including real-gas effects. Namely, the N-factor envelope shown in Figure 9 of Ref. [7] for the case of m=13.5 g/s has the same qualitative behavior as the envelope of black lines in Figure 13.

IV. Shaping of the injector

The foregoing stability analysis suggests that the injector performance may be improved by shaping of the injection region. It was suspected that decreasing of the injector surface slope can partially compensate the displacement effect induced by the blowing and, presumably, reduce the instability growth in the relaxation region. This speculation was examined by parametric stability studies of the following configurations.

The first configuration is a conical shape schematically shown in Figure 14. The rear part of the original cone ($x^* > 169$ mm) is shifted along the x-axis to Δb^* , and it is connected with the fore part through a conical surface (red line), which is used for injection. The angle of the new injector surface decreases from $\theta_c = 5^\circ$ to $\theta_c - \Delta \theta$ and its x-length increases from $b^* = 41$ mm to $b^* + \Delta b^*$. Stability computations were performed for the injector shapes corresponding to $\Delta \theta = 1^\circ$ and 3° . The total mass rates were m = 0, 6.75 and 13.5 g/s for each shape.

The second configuration has the injector of cylindrical shape shown in Figure 15. In this case $\Delta \theta = 5^{\circ}$, the injector length is 41 mm and stability computations were performed at m = 0, 1.35, 4.05, 6.75, 9.45 and 13.5 g/s.

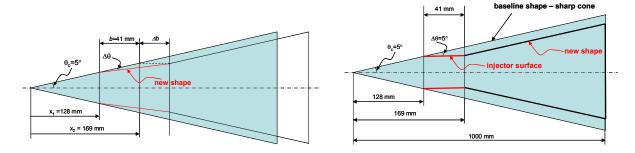


Figure 14. Conical shaping of the injection region.

Figure 15. Injector of cylindrical shape.

A. Conical injectors

Stability computations for the conical shapes of $\Delta\theta=1^\circ$ and 3° at zero blowing showed that the injector shapes weakly affect the N factors of the Mack mode. As an example, Figure 16 compares the distributions of N(x) for the baseline case (straight cone) with the case of $\Delta\theta=3^\circ$. These distributions are very similar showing that the shaping did not affect transition by itself.

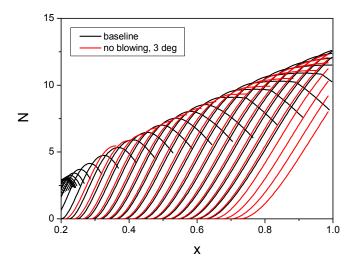


Figure 16. N-factors of the Mack mode for the straight cone (black lines) and for the shape of $\Delta\theta=3^\circ$ (red lines) at $m=0\,$ g/s.

Now we consider the baseline configuration ($\Delta\theta=0^\circ$) and the conical injectors of $\Delta\theta=1^\circ$ and 3° at the injection mass rate m=13.5 g/s. Figures 17 and 18 compare the basic flow fields for static pressure and axial velocity, respectively. As expected, the injector shaping reduces the pressure perturbations induced by the boundary-layer displacement. However, the thickness of dead-flow layer and, as a consequence, the length of relaxation region increase with increasing of $\Delta\theta$.

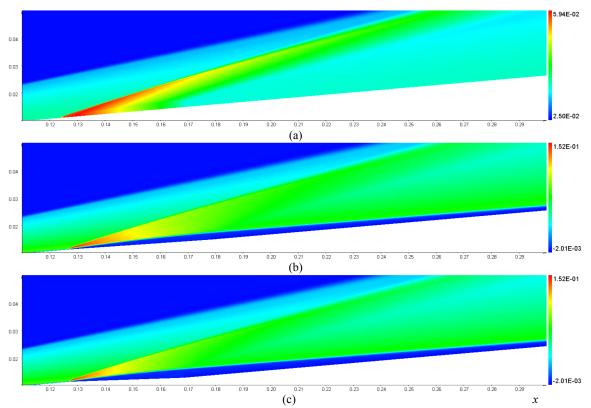


Figure 17. Mean flow fields for the nondimensional static pressure at the total mass flow rate $m=13.5\,$ g/s; (a) $-\Delta\theta=0^{\circ}$ (baseline cone), (b) $-\Delta\theta=1^{\circ}$, (c) $-\Delta\theta=3^{\circ}$.

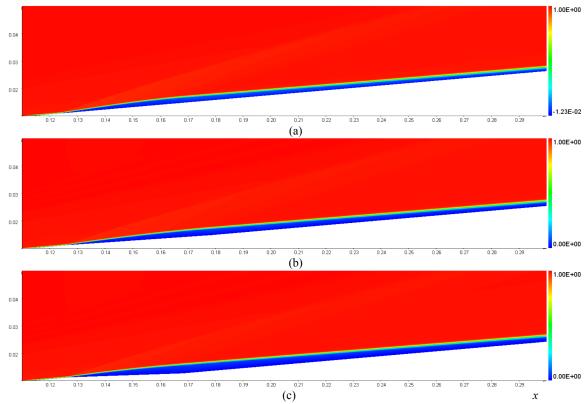


Figure 18. Mean flow fields for the nondimensional axial velocity at the total mass flow rate $m=13.5\,$ g/s; (a) $-\Delta\theta=0^{\circ}$ (baseline cone), (b) $-\Delta\theta=1^{\circ}$, (c) $-\Delta\theta=3^{\circ}$.

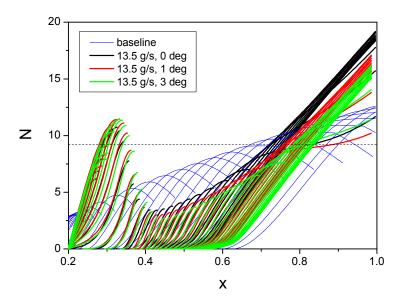


Figure 19. N-factors of the Mack mode for the straight cone with zero blowing (blue lines, baseline case), for injectors of $\Delta\theta=0^\circ$ (black lines, cone with blowing), $\Delta\theta=1^\circ$ (red lines) and $\Delta\theta=3^\circ$ (green lines) at $m=13.5\,$ g/s; dashed line – $N_{tr}=9.2\,$.

Figure 19 shows the Mack mode N-factors computed for the mean flows presented in Figures 17 and 18. It is seen that the injector shaping produces a weak destabilization effect in the near-field relaxation region

0.2 < x < 0.4 and a noticeable stabilization effect in the mid-field and far-field relaxation regions. Because the near-filed maximum of the N-factor envelope remains to be higher than N_{tr} , these injectors may cause premature transition.

B. Cylindrical injector

Figure 20 shows the nondimensional wall-pressure distributions $P_{\mu\nu}(x)$ of the mean flow for different injection rates m from 0 to 13.5 g/s. The dashed lines correspond to the injection boundaries. The baseline distribution on a straight cone without injection is approximately uniform (the solid black line). The shaping without blowing (the red line) leads to the pressure drop on the injector surface. This behavior is consistent with the slender body theory for inviscid flows. The blowing causes a sharp increase of $P_{\scriptscriptstyle w}$ near the upstream boundary of the injector. Then $P_{\scriptscriptstyle w}$ decreases to the level, which is lower than in the baseline case. Further downstream the wall pressure is almost constant in the relaxation region. The length of P_{w} plateau increases while its level decreases as the injection mass flow rate increases. These mean-flow changes affect the maximal (vs. frequency) growth rates of the Mack mode as shown in Figure 21. The shaping itself (red line for the case of m=0) weakly affects the distribution of σ_{max} . As m increases, a sharp peak of $\sigma_{\max}(x)$ is formed near the upstream boundary of injection (at $x \approx 0.13$). Another maximum is observed in the relaxation region. Because its location is shifted downstream with m, the injection affects the N-factor distributions in a nontrivial manner (Figure 22). The first maximum of the N-factor envelope (which is located in the near-field relaxation region) increases with m, while the region of steep envelope (which is located in the far-field relaxation region) is shifted downstream. Because the N-factor envelopes are non-monotonic vs. x^* , the e^N method predicts different transition onsets depending on the choice of critical N. For $N_{tr}=9.2$ (horizontal dashed line), the most promising cases are related to m = 6.75 - 9.45 g/s. More studies would be needed to account for the non-relaxation effects in the far region.

Figures 23a and 23b compare the N-factors for the cases of $\Delta\theta=0^\circ$ (cone without shaping) and $\Delta\theta=5^\circ$ (cylindrical injector) at $\dot{m}=6.75\,$ g/s and 13.5 g/s, respectively. Although the cylindrical injector works better in the mid-field and far-field relaxation regions, its performance is not improved in the most critical near-filed region where the N factor envelope has a local maximum.

Thus, the e^N analysis suggests that the considered herein shaping does not prevent from early transition in the near-field relaxation region at sufficiently large injection rates (e.g., Figure 23b). For relatively small m at which N-factors in the near-field region are below the critical level (e.g., Figure 23a), the shaping produces a significant stabilization effect on the boundary layer in the mid- and far-field regions.

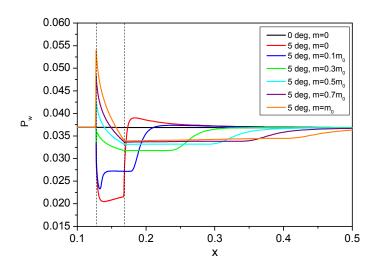


Figure 20. The mean-flow wall-pressure distributions in the region $0.1 \le x \le 0.5$ at the total mass rate from 0 to 13.5 g/s; black line – baseline case of straight cone without injection, dashed lines show the injection boundaries.

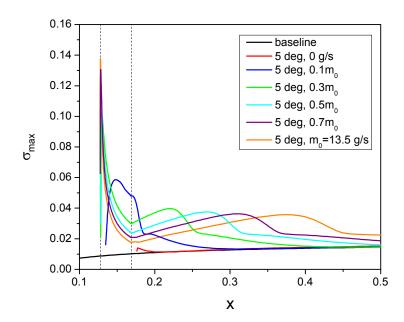


Figure 21. Maximal (vs. frequency) growth rates of the Mack mode. Black line – baseline case of straight cone with zero injection. Colored lines – cone-cylinder-cone configuration with different injection mass flow rates from 0 to $m_0=13.5\,$ g/s. Dashed lines show the boundaries of injection. $\sigma_{\rm max}$ is made nondimensional using the Blasius length scale $\sqrt{\nu_e^*x^* / U_e^*}$.

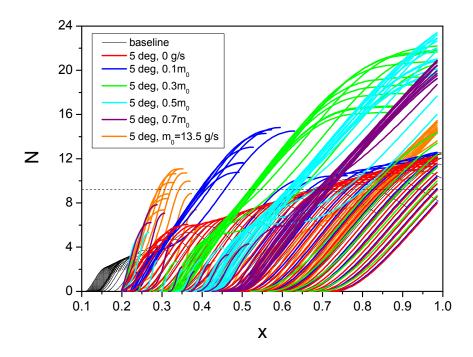


Figure 22. N-factors of the Mack mode for the cylindrical injector ($\Delta\theta=5^\circ$) at different injection mass rates from 0 g/s to $m_0=13.5\,$ g/s; dashed line – $N_{tr}=9.2$.

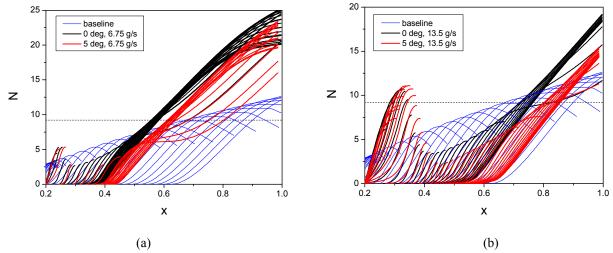


Figure 23. N-factors of the Mack mode for the straight cone with zero blowing (blue lines, baseline case), for injectors of $\Delta\theta=0^\circ$ (black lines, cone with blowing) and cylindrical injector with $\Delta\theta=5^\circ$ (red lines). (a) – the injected mass rate is $m=6.75\,$ g/s, (b) – $m=13.5\,$ g/s; dashed line – $N_{tr}=9.2\,$.

V. Suction-blowing of zero mass injection

Another way to improve the injector performance could be a combination of normal-wall suction and blowing with zero net injection as schematically shown in Figure 24. It is expected that the preliminary suction of the incoming boundary-layer flow could partially compensate negative effects produced by the subsequent blowing.

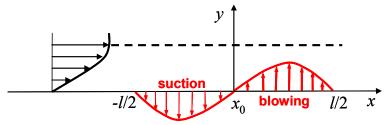


Figure 24 Schematics of suction-blowing of zero net injection.

This expectation is examined by stability computations for the following distribution of suction-blowing. In the injection region $-l^*/2 \le x^* - x_0^* \le l^*/2$, where $x_0^* = 212.5$ mm is the injector center and $l^* = 41$ mm, the mass-flow rate $q = \rho_w v_w$ is specified as

$$q(\varphi) = q_0 \, \frac{l}{2\pi} \sin \varphi, \, \varphi = (x - x_0) 2\pi \, / \, l, \, \, -\pi \le \varphi \le \pi \, . \label{eq:qphi}$$

In this case the suction mass flow rate is

$$m_{_{-}} = q_{_{0}} \frac{l}{2\pi} \int\limits_{_{-\pi}}^{^{0}} \sin z dz = -q_{_{0}} l \: / \: \pi \: , \label{eq:m_prob}$$

the injection mass rate is

$$m_{_{+}}=q_{_{0}}\frac{l}{2\pi}\int\limits_{_{0}}^{\pi}\sin zdz=q_{_{0}}l\,/\,\pi\;,$$

so that the net mass flow rate is zero, $m_+ + m_- = 0$. Computations were performed for $m_+ = 6.75\,$ g/s (a half of maximal injection mass rate considered in the previous sections). The mean flow field for static pressure, axial velocity and temperature are shown in Figure 25. Figure 26 compares the wall pressure distributions for the baseline

(no-blow) case, the uniform blowing of m=6.75 g/s and the suction-blowing of $m_+=6.75$ g/s. It is seen that in the suction-blowing case the relaxation region is shorter and the dead-flow layer is thinner than in the case of uniform blowing. However the local perturbations in the vicinity of suction-blowing system are quite large.

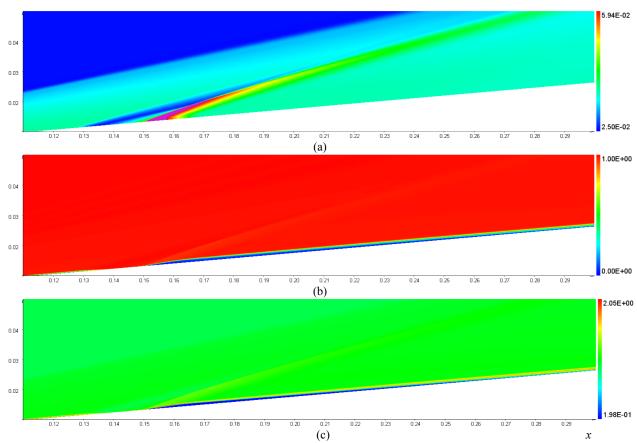


Figure 25. Basic flow fields for the nondimensional static pressure (a), axial velocity (b), and temperature (c) at $m_{\perp}=6.75$ g/s.

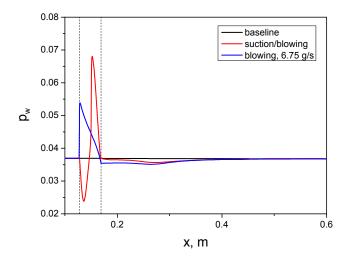


Figure 26. The wall pressure distributions for the baseline (no blow) case (black line), the uniform blowing of m=6.75 g/s (blue line) and the suction-blowing of $m_+=6.75$ g/s (red line).

Figure 27 shows N factors corresponding to the cases in Figure 26. As contrasted to the original expectation, the suction-blowing system destabilizes the flow compared with the uniform blowing case. Thus, the preliminary suction does not improve the injector performance.

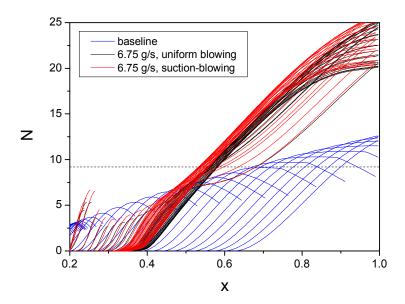


Figure 27. N-factors of the Mack mode for the baseline (no-blow case), the uniform blowing of m=6.75 g/s (black line) and the suction-blowing of $m_+=6.75$ g/s (red line); dashed line – $N_{tr}=9.2$.

VI. Conclusions

Stability analyses of high-speed boundary-layer flow past a 5° half angle sharp cone with the wall-normal injection of gas through a porous strip were performed using Navier-Stokes solutions for the mean flow and the linear stability theory. The configuration and free-stream parameters were chosen to be similar to the experiments, which were carried out at Caltech's T5 shock tunnel to investigate the effect of CO₂ injection on laminar-turbulent transition.

It was found that the injection induces a cold dead-flow layer, which is slowly swallowed by the shear layer in the downstream relaxation region. The near-wall flow behaves as a wave guide which can support several unstable modes of acoustic type. The spatial stability analysis showed that the most unstable mode corresponds to the Mack second mode. The phase speeds of this instability are close to the phase speeds of slow acoustic waves in the free-stream, and its frequencies are several times smaller than in the no injection case. This may lead to dramatic increase of receptivity to free-stream noise.

The e^N computations showed that the injection leads to destabilization of the near-field region, stabilization of the mid-field relaxation region, and destabilization of the far-field relaxation region where the basic flow is almost parallel. However, the results obtained here are most applicable to the near-field region where the perfect gas assumption is valid. The width and location of these regions as well as the level of stabilization/destabilization effect essentially depend on the injected mass flow rate. These results are consistent with the stability computations of Wagnild et al. [7], which were carried out for CO₂ injection including the real-gas effects.

In order to improve the injector performance it was suggested to decrease the injector surface slope. It was suspected that this shaping could partially compensate the displacement effect induced by the injection and thereby reduce the instability growth in the near-field relaxation region. However, the e^N parametric computations predicted that this shaping does not stabilize the near-field flow and, therefore, it does not prevent from early transition at sufficiently large injection rates. For relatively small injection rates, at which the N-factors in the near-field region are below the critical level, the shaping produces a significant stabilization effect in the mid- and far-field regions. It is expected that this stabilization will be strongly enhanced by the injection of CO₂.

It was also suspected, that the injector performance could be improved using a combination of normal-wall suction and blowing with zero net injection. It was assumed that the preliminary suction of the incoming boundary-

layer flow could partially compensate negative effects produced by the subsequent blowing. However, the e^N computations showed that the suction-blowing system destabilizes the flow in the whole relaxation region.

It should be noted that the local injection induces spatial non-uniformities of the basic flow, which can alter the instability growth rates via nonparallel effects. Because our stability analysis does not account for these effects, the foregoing results should be taken with great caution. The PSE analysis and direct numerical simulations are needed to verify the e^N predictions reported herein. Note also that the perfect gas model does not account for the CO_2 stabilization effect owing to absorption of acoustic energy. This model is suitable for the near-filed region where the injected gas is relatively cold and the absorption effect is weak. Further downstream, where the injected flow is heated, the perfect gas model overestimates the disturbance growth rates and, presumably, under-predicts the injector performance. Nevertheless, the perfect gas modeling provides a good launching pad for further stability analysis including the real gas effects.

Acknowledgments

This work was supported by the European Office of Aerospace Research and Development via the US Civilian Research and Development Foundation, grant CRDF-31107-MO-12.

References

- 1. Mack, L.M., "Boundary-Layer Stability Theory," In Special Course on Stability and Transition of Laminar Flow, AGARD Report Number 709, 1984.
- 2. Fedorov, A., "Transition and Stability of High-Speed Boundary Layers," *Annu. Rev. Fluid Mech.*, Vol. 43, 2011, pp. 79-95.
- 3. Lighthill, M.J., "Viscosity Effects in Sound Waves of Finite Amplitude," In G.K. Batchelor and R.M. Davies, editors, Surveys in Mechanics, pp. 250-351. Cambridge University Press, 1956.
- 4. Vincenti, W.G. and Kruger, C.H. Introduction to Physical Gas Dynamics, Krieger Publishing Company, 1965.
- 5. Fujii, K., and Hornung, H. G., "Experimental Investigation of High Enthalpy Effects on Attachment-line Boundary Layer Transition," *AIAA J.*, Vol. 41, No. 7, July 2003.
- 6. Leyva, I. A., Jewell, J. S., Laurence, S., Hornung, H. G., Shepherd, J. E., "On the Impact of Injection Schemes on Transition in Hypersonic Boundary Layers," AIAA-2009-7204, October 2009.
- 7. Wagnild, R.M., Candler, G.V., Leyva, I.A., Jewell, J.S., and Hornung, H.G., "Carbon Dioxide Injection for Hypervelocity Boundary Layer Stability," AIAA-2010-1244, January 2010.
- 8. Jewell, J.S., Leyva, I.A., Parziale, N.J., and Shepherd, J.E., "Effect of Gas Injection on Transition in Hypervelocity Boundary Layers," ISSW, July 2011.
- 9. Egorov, I.V., Fedorov, A.V., and Soudakov, V.G., "Direct Numerical Simulation of Disturbances Generated by Periodic Suction-Blowing in a Hypersonic Boundary Layer," *Theor. Comput. Fluid Dyn.*, Vol. 20, No. 1, 2006, pp. 41-54.
- 10. Egorov, I.V., Fedorov, A.V., and Soudakov, V.G., "Receptivity of a Hypersonic Boundary Layer over a Flat Plate with a Porous Coating," *J. Fluid Mech.*, Vol. 601, 2008, pp. 165-187.
- 11. Fedorov, A.V., Soudakov, V.G., and Egorov, I.V., "Investigations of Laminar-Turbulent Transition on a Sharp Cone with Localized Heating or Cooling in High-Speed Flow," AIAA-2013-0524, January 2013.
- 12. Fedorov, A.V., "Receptivity of a Supersonic Boundary Layer to Solid Particulates," *J. Fluid Mech.*, vol. 737, 2013, pp. 105-131.
- 13. Jiang, G.-S., and Shu, C.-W., "Efficient Implementation of Weighted ENO Schemes," *J. Comput. Phys.*, Vol. 126, 1996, pp. 202-228.